communications materials

A Nature Portfolio journal

Article

https://doi.org/10.1038/s43246-025-00910-3

Defect-modulated ionic friction at hBN/water interfaces

Menghua Zhao [1,2], Kenji Watanabe [3], Takashi Taniguchi [4] & Jean Comtet [1]

Charge transport at solid/liquid interfaces is vital to energy conversion, electrochemistry, and biological activities. These buried interfaces are the locus where continuum approaches break down, and molecular details become of utmost importance, with traditional ensemble-averaged studies giving an incomplete picture of the dynamics. Here, we build upon recently developed single-molecule microscopy optofluidic platform, to investigate the statistics of single charge transport at aqueous hexagonal Boron Nitride interfaces, demonstrating the microscopic origin of its non-Gaussian character and the control of transport by irradiation-induced surface defects. By increasing irradiation of the hBN crystals, we modulate the morphological distribution of adsorption sites, leading to a slow-down of interfacial charge transport, akin to an increasing frictional interaction. Charge hopping displacements feature exponentially-decaying arms, strongly departing from Gaussian distributions. 2D Brownian dynamics simulations evidence that these exponential tails originate from molecular jumps between trapping sites, allowing a consistent match between statistical distributions and the effective diffusion coefficient. Our study highlights the key yet overlooked role of defects in regulating interfacial charge transport, with relevance for energy applications.

Ionic transport at the solid/liquid interface is ubiquitous both in natural settings and industrial applications, and is crucial for a large number of domains ranging from biology[1,2], blue energy conversion[3,4], filtration[5,6], up to electrochemical and catalytic reactivity[7]. Interfacial transport accordingly stands at the crossroad where continuum descriptions meet with the molecular granularity of the interface. Molecular details related to the solid surface can accordingly have massive impacts on interfacial transport. Versatile experimental toolboxes, including vibrational sum frequency generation spectroscopy[8,9], electrokinetic detection[10,11] and atomic force microscopy[12,13] have been developed to study the nanoscale ion and liquid transport at the interface, revealing new physical phenomena, such as fast flow in carbon nanotubes[14], high selectivity of biological ion channels[5,6] or giant energy conversion rate[3,15]. However, despite substantial progress in recent years, the molecular processes underlying ionic transport at interfaces remain elusive due in part to experimental challenges associated with the direct observations of ion and solvent transport at the molecular scale[16–18]. Conventional techniques, including the aforementioned ones, mostly employ indirect measurements, detecting ensemble quantities that are temporally and spatially averaged. Those macroscopic fluxes lose precise information related to the temporal and spatial details of single-molecule dynamics[19]. In particular, while non-Gaussian processes at liquid–solid interface have long been recognized for single particle transport[20–23], the generalizability of these observations to single-charge and single-ion dynamics, as well as the microscopic origin of such peculiar transport, remains poorly understood. Finally, recent advancement in nanofluidics has further pushed the confinement of the liquid transport down to one single molecule size[5,6,18], a situation where continuum approaches are clearly breaking down[16,24,25], calling for an urgent understanding of the interfacial ion transport at the single molecular scale[16,17,25,26].

Following the recent discovery of defect-induced solid-state emitters in hexagonal Boron Nitride (hBN) materials[27], visualization of interfacial charge transport has recently become a reality[28–30]. The emergence of fluorescent sensors based on quantum emission of hBN defects opens new routes to study the interfacial transport at the single molecular scale in a label-free way[29,30]. Thanks to its large band gap of ~6 eV, the hBN can host perturbed energy states created by surface defects that can be optically activated by an external light excitation at room temperature[31]. This peculiar property has recently been shown to grant the hBN unprecedented ability for direct label-free readout of charge and ionic exchanges with the solvent[30,32,33] or biomolecule adsorption[34]. Emergent studies have been carried out with this technique to reveal the proton transport pathway[30], physiochemical adsorption[32,35] and electrochemical kinetics[36] at the interface.

---

[1]Laboratory of Soft Matter Science and Engineering, ESPCI Paris, PSL University, Sorbonne Université, CNRS, Paris, France. [2]School of Information Mechanics and Sensing Engineering, Xidian University, Xi'an, China. [3]Research Center for Electronic and Optical Materials, National Institute for Materials Science, Tsukuba, Japan. [4]Research Center for Materials Nanoarchitectonics, National Institute for Materials Science, Tsukuba, Japan. e-mail: jean.comtet@espci.fr

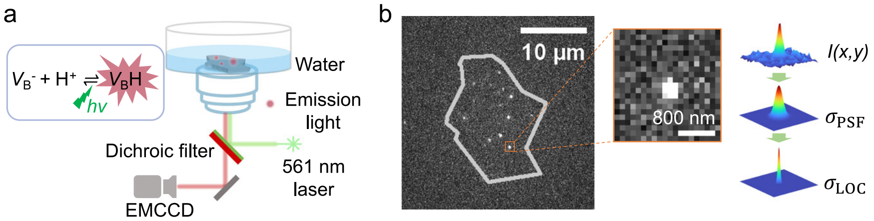

Fig. 1 | Single-molecule imaging of optically active defects. a Schematics of the single-molecule fluorescence microscopy setup. hBN flakes with optically active defects (red emission point) are exfoliated onto the glass coverslip and put in contact with water. The fluorescent quantum emission from hBN defects is triggered by excitation through a 561 nm laser and projected onto an EMCCD camera. The inset illustrates the envisioned acid-base charge transition between non-emissive defects in the negatively charged V_B^- form and fluorescent defects in the protonated V_BH form[30]. **b** Principle for emitter super localization, showing a wide field image of a hBN flake with the flake edge indicated by the grey line, and a diffraction-limited white spot identified as single-molecule emission. As shown in the inset, the 2D spatial intensity profile can be approximated by a Gaussian Point Spread Function of width σ_{PSF}, allowing for a final uncertainty in the center position as $\sigma_{LOC} \approx \sigma_{PSF}/\sqrt{n}$ with n the number of emitted photons.

Following these preliminary achievements, it now appears of particular interest to understand the role of the structural properties of the solid surface, such as the presence and distribution of defects—inevitable in real-world materials—on interfacial charge transport and ionic friction. Defects have indeed been suggested to play a central role in determining interfacial molecular transport in nanofluidics[24,37–41], with reports of the influence of defect size[24], reactivity[38] and chemical structure[39] on the solid/liquid friction. However, most of these studies stay at the conceptual level in the context of simulations, lacking convincing direct experimental proofs.

Here, we use single-molecule tracking techniques to study the statistical properties of single proton transport on the aqueous hBN interface and further address their control with surface defects. By tuning the defective state through mild plasma treatments, we first evidence two morphologies of adsorption sites. Focusing on charge dynamics, we report a generic non-Gaussian yet Fickian process for single charge diffusion and subsequently demonstrate the strong role of surface defects in setting transport properties. To rationalize these observations, we perform ad hoc simulations of Brownian particles undergoing free 2D Brownian diffusion in a defective landscape. Adsorption at defect sites is modelled explicitly and treated as emission events, allowing for a direct comparison with our experimental distributions. Remarkably, both our experiments and Brownian dynamics simulations evidence an exponential scaling for the elementary jumps. Such peculiar distributions originate from the hopping of charge between the surface defects, highlighting the molecular origin of this non-Gaussian surface transport process. The diffusion coefficient on the plasma-modified defect state is accordingly strongly set by such adsorption events, allowing us to consistently match these statistical distributions with the effective diffusion coefficient by a scaling law arising from the desorption-mediated transport. Our study sheds light on the molecular origin of the non-Gaussian interfacial distribution for ionic transport and provides new insights on the role played by surface defects in the interfacial charge transport: the greater the density of surface defects, the lower the interfacial diffusion coefficient and the higher the effective frictional interactions felt by the surface trapped charges. Our study finally suggests that a simple tuning of the defect density offers an alternative way of regulating liquid and charge transport in the applications of battery design, clean energy conversion and desalination.

Results and discussion

Experimental methodology for single proton tracking

To access interfacial molecular transport at the single-charge level, we harvest the quantum fluorescent emission originating from hBN surface defects[27] and their peculiar interactions with liquids[28–32]. Atomically smooth hBN multi-layers are first mechanically exfoliated from bulk crystals on transparent glass coverslips. Subsequent air plasma etching is performed using a plasma cleaner (Femto Science Cute, Femto Science Inc., Korea) with the following settings: gas time 15 s, base pressure 0.15 Torr, process pressure 0.5 Torr, plasma power 10 W, generation frequency 50 kHz and purge time 15 s. This treatment induces fluorescent surface defects that are activated in contact with aqueous solutions[28,29,35] once excited in wide-field by a green laser (561 nm), with fluorescent emission at ~585 nm[29]. Fluorescent emission is subsequently imaged on a low-noise EMCCD camera via an ×100 oil-immersion microscope objective, shown in Fig. 1a. The incident excitation light is removed from the light path by dichroic and emission filters, allowing only the emitted light to be effectively captured by the camera sensors (see Methods). Based on previously reported pH dependence of the fluorescence emission and ab-initio molecular dynamics simulations[30], a potential mechanism responsible for the quantum emission, is presented in the inset of Fig. 1a, where the non-emissive negatively charged boron monovacancy defect, V_B^-, can react with surrounding solvated aqueous protons, leading to the transition towards a fluorescent protonated defect V_BH. By spatially and temporally tracking the correlated emission events, we are able to dynamically probe proton charges walking on hBN surfaces.

The typical fluorescence signal consists of diffraction-limited spots resulting from the activation of single defects, as shown in Fig. 1b. To localize the position of these emitters below the diffraction limit, we fit their point spreading function (PSF) by integrated 2D Gaussians, allowing for the subsequent localization of their position with nanometric resolution[42]. The localization uncertainty is estimated by $\sigma_{LOC} \approx \sigma_{PSF}/\sqrt{n}$, with σ_{PSF} the standard deviation of the Gaussian fit and n the number of photons received by the camera. The camera exposure time, Δt, was set at 20 ms during all the recordings if not specifically specified. The trajectories were tracked via spatially and temporally correlating neighboring defects with the maximum displacement, $\Delta l = 1$ μm, allowing the detection of diffusion coefficient up to $\Delta l^2/(4\Delta t) \approx 10^{-11}$ m^{2}s^{-1}. All experiments were performed using Milli-Q purified water for a total duration of 10,000 frames, with approximately tens of thousands of localizations and several thousand trajectories recorded for each observation.

The causal nexus for our trajectory analysis is legitimized on the basis of the large difference between the local hopping distances over which we evidence correlated motion (at most 1 μm) and the typical distance between active fluorescent sites present at each frame (larger than 5 μm). As such, our assertion regarding the observation of trajectories and spatiotemporal correlations is further supported by a shuffling analysis of the recorded image sequences (see Supplementary Fig. 1), which demonstrates that the trajectory-like correlations observed in the original data vanish when the temporal order of frames is randomized.

We further argue that transport between defects occurs through bidimensional diffusion of protons at the interface, consistent with the presence of a physisorption energy well in the vicinity of the aqueous hBN surface, as evidenced by previous simulations[30,43]. Experimentally, we note that (1) the mean distance travelled by a proton in solution during a single frame exposure is $\sqrt{D_{bulk}\Delta t} \sim 100$ μm, a distance far greater than the lateral dimensions of the hBN flakes (~10–20 μm) and (2) the mean distance between free protons close to the hBN surface is of the order of 180 nm at pH of 5. If a proton were to

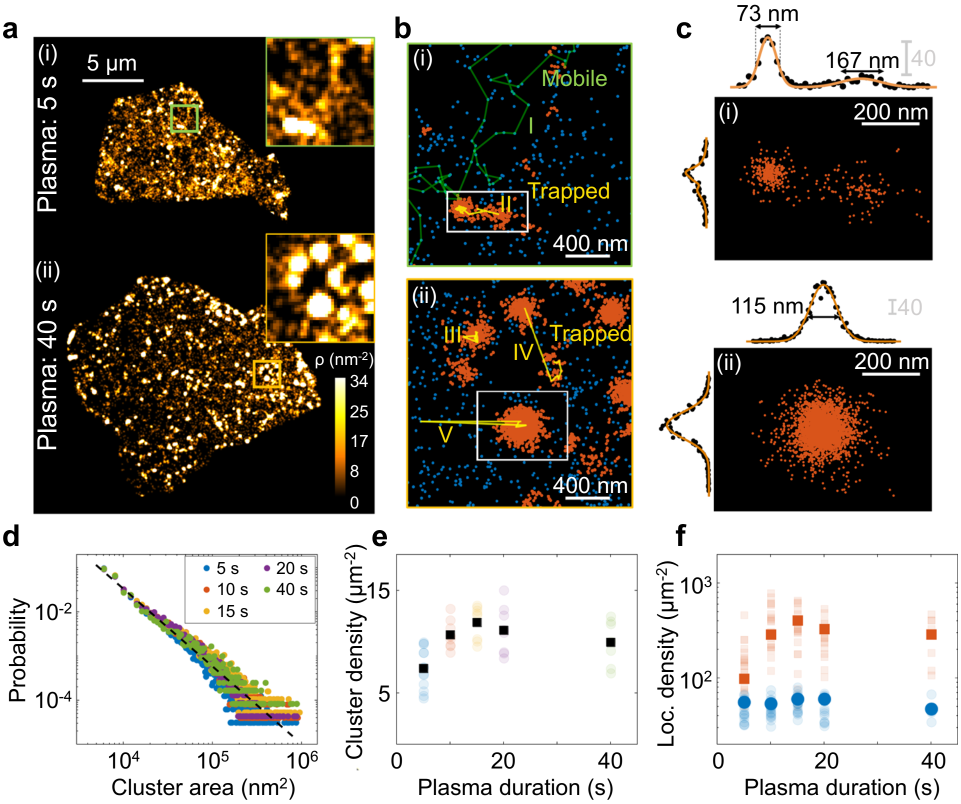

Fig. 2 | Spatial localization of emissive defects. **a** Heat map of active emissive sites on hBN flakes with t_{plasma} of 5 s (i) and 40 s (ii), respectively. Visualization of localization events is based on a density function, ρ, using the averaged shifted histograms[58] with the bin size of 114 nm × 114 nm. Insert images, 2 μm × 2 μm, are the zoom-in of the region of interest (ROI) randomly selected. **b** Localization details of the ROI on (**a**). Red and blue dots correspond to the adsorption events inside the cluster island and the sparse zone, respectively. The solid lines indicate the traveling trajectory of single protons with associated trajectories labeled from I to V. **c** Distributions of localization events in the rectangle marked in (**b**). The scale bar close to the distribution curve corresponds to the number of localization events within each bin of width 10 nm. The solid lines are Gaussian fittings to the clusters with their FWHM indicated by arrows. **d** Ensemble distribution probability of the cluster area at various t_{plasma} from 5 s and 40 s, defined as the ratio of the number of clusters within a given area bin to the total number of clusters. The dashed line shows a power law with the power exponent of −1.8. Bin size: 2000 nm^2. **e** Cluster density on flakes at different t_{plasma}. Each data point corresponds to the observation on a single hBN flake. The black solid square is the average of all observations at each t_{plasma}. **f** Localizations density inside clusters (trapped, red color) and outside clusters (mobile, blue) on fakes at various t_{plasma}. Each data point corresponds to the observation on a single hBN flake. The bold solid point is the average of all observations at each t_{plasma}.

leave the interface after desorption from a first defect, it would thus become instantaneously indistinguishable compared with the other nearby proton. As this indistinguishability would be in contradiction with our observations of trajectories, the observed correlations in the activation of nearby sites in our system thus imply restricted exchanges between the surface and the bulk in our experimental system, characterized by 2D interfacial charge transport. Yet we acknowledge that obtaining direct experimental evidence regarding 2D versus 3D transport would require measuring the distribution of time it takes for protons to go from one site to the other, comparing them with first-passage times for 2D or 3D diffusion[9,44,45]. Unfortunately, measuring such quantities would require temporal resolutions of microseconds for the monitoring of emitter dynamics[30,35], which is out of reach of current experimental approaches at the single-molecule scale.

A qualitative description of active defect distribution and proton dynamics

We first report in Fig. 2 on the effect of plasma treatment on the spatial distribution of active defects. The subsequent activation and localization of fluorescent defect sites over a large number of frames can be used to create super-resolved maps in which each point corresponds to the position of one optically active site, equivalent to one proton charge adsorption event. We show in Fig. 2a such images reconstructed from 10,000 frames for two plasma treatment durations, t_{plasma}, of respectively 5 s (i) and 40 s (ii). As shown by the zoom-ins of Fig. 2a, the spatial distribution of defect activation is highly heterogeneous, with high intensity spots corresponding to high densities of localization events, coinciding with sparser localizations. Such observations are consistent with previous reports in which a similar plasma treatment was applied[28,29,35]. Here, we refine these qualitative observations by performing quantitative clustering analysis, using an inter-localization threshold distance D_l of 20 nm (more details in Supplementary Fig. 2), allowing us to disentangle clusters from sparse localizations. Results of this clustering approach are shown in Fig. 2b, where clustering localizations are shown as red dots, while the sparse localizations appear in blue. Fig. 2c reveals the detailed structure of single clusters (additional examples in Supplementary Fig. 2). Clusters are of either one single strong adsorption zone (ii) or multiple strong adsorption zones (i). The cluster consists of tens to hundreds of adsorption events, resulting from persistent adsorptions from alternative charges on various trajectories at different time frames (Supplementary Fig. 3). To characterize whether these sites actually correspond to groups of defects, or result from localization uncertainties of a single defect active over many frames, we computed their Full Width at Half Maximum, FWHM characterizing the spatial spread of these clusters. As shown in Fig. 2c (additional examples in Supplementary Fig. 2), the FWHM can reach up to 200 nm, a value much higher than the localization uncertainty expected for a single defect, pointing to the fact that clusters do correspond to dense regions carrying distinct defects. Note, however, that due to the finite localization precision of our setup, we are unable to access the actual defect distribution inside clusters.

Based on this clustering methodology, we can analyze in more detail the effect of plasma treatment on the defect density and cluster morphology. We first report in Fig. 2d, the distribution of cluster area for various t_{plasma}. This distribution follows an approximate power-law distribution, with a scaling ~1.8, characterizing the large spread in cluster size. We hypothesize that such broad distribution is a signature of a complex cluster creation regime, proceeding from local nucleation and growth at highly damaged regions. Despite the apparent independence of the cluster size on irradiation time demonstrated in Fig. 2d, we evidence in Fig. 2e, f a clear effect of plasma duration on cluster density and localization density, which monotonically increases up to $t_{\text{plasma}} = 15$ s. The saturation at high t_{plasma} might be associated with a shift from emissive to non-emissive defects upon continuous irradiation through an exact mechanism which remains to be properly addressed. It should be noted that varying the critical length used to define the cluster results in slight alterations to the reported cluster area, but does not affect the aforementioned trends.

We now turn in Fig. 3 to the discussion of the proton dynamics on such defective landscapes. A remarkable feature of the defect activation dynamics is the subsequent time-correlated activation of nearby defect sites, consistent with the transport of a single activating species along nearby defect sites.

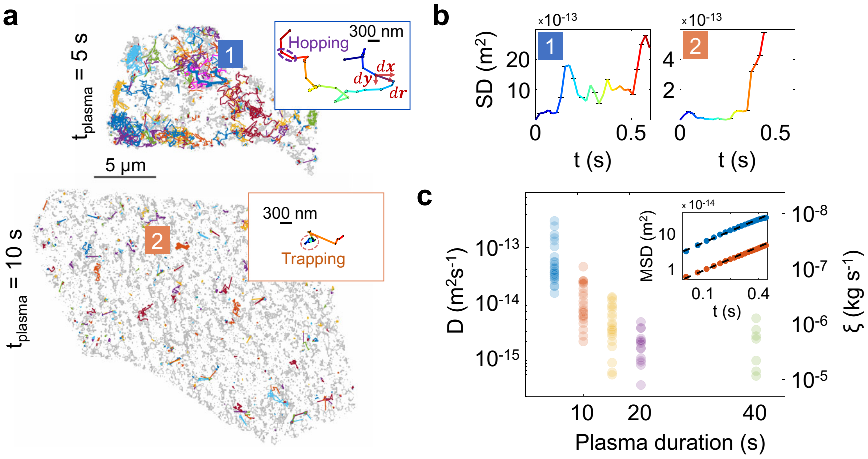

Fig. 3 | Effect of the surface defects on proton dynamics. a Summary of one-half of the ensemble trajectories longer than four frames superimposed together from 10,000 frames' recording at two t_{plasma} of 5 s (top) and 10 s (bottom). The insert: zoom-in of the trajectories 1 and 2 corresponding to the ones highlighted in blue and orange, respectively. Trapping and hopping events are defined by a critical displacement between the adjacent two hopping events, below which the "Trapping" event is defined and above which the "Hopping" event is defined. The circle on the trajectory indicates the localization uncertainty; $d\mathbf{r}$, dx and dy denote the displacement, x-displacement and y-displacement between the adjacent emission events, respectively, with $|d\mathbf{r}| = \sqrt{|dx|^2 + |dy|^2}$. **b** Single trajectory square displacement for the cases on (**a**) at t_{plasma} of 5 s and 10 s, respectively. t denotes the time and $t = 0$ indicates the beginning of each trajectory. **c** Diffusion coefficient D and friction coefficient ξ of protons at aqueous hBN interfaces from ensemble MSD as a function of t_{plasma}. Each data point comes from independent measurement from one single flake. The insert: ensemble trajectory mean square displacement for the cases on (**a**) at t_{plasma} of 5 s and 10 s, respectively. The averaged diffusion coefficient D is extracted from the linear fit for the initial 0.4 seconds.

Given the strong dependence of the distribution of activated defects on plasma treatment, as shown in Fig. 2, it is intriguing to ask whether a similar dependence may be observed on the interfacial charge dynamics. To further elucidate this point, we performed single-molecule tracking on surfaces subjected to different plasma treatments. Figure 3a depicts ensemble maps of one half of trajectories longer than four frames, for two distinct plasma irradiation time: 5 seconds (top panel) and 10 seconds (bottom panel). One concurrent feature is that proton charge trajectories exhibit intermittent kinetics with many of them shifting between the mobile state (hopping) and the immobile state (trapping), as demonstrated by the trajectories (1) and (2) in the insert of Fig. 3a. Meanwhile, individual trajectories show significant heterogeneity: some remain almost immobile (trajectory (2)), while others exhibit high mobility (trajectory (1)). We clearly observe a large number of mobile trajectories for $t_{plasma} = 5$ s in Fig. 3a, while that is not the case for $t_{plasma} = 10$ s. A detailed correlation between the dynamical trajectories and the localizations is present in Fig. 2b. Two types of trajectory modes are revealed at short t_{plasma} of 5 s in Fig. 2b(i). Single protons either travel in an intermittent way in the sparse zone (Hopping mode) or is entirely adsorpted onto the clusters (Trapping mode). Those observations do not stick for the cases at longer t_{plasma} where more and more charges are locally trapped and eventually the majority become trapped at extreme t_{plasma}. As manifested by the Fig. 2b(ii), protons are strongly adsorbed onto cluster sites and exhibit limited mobility, demonstrated by the typical trajectories III-V where protons mostly stroll inside cluster sites (trajectory III, adsorption) and rarely jump between cluster sites (trajectories IV-V, hopping).

To address the observations above in a more quantitative way, we follow a traditional route by using the square displacement $\mathrm{SD}(t) = \langle|\mathbf{r}(t) - \mathbf{r}(t=0)|^2\rangle$ to account for the dynamics at the single molecule scale. As evidenced in Fig. 3b, the squared displacement calculated on individual trajectories shows pronounced fluctuations associated with the successive transitions between trapping and hopping states. In order to offset the large discrepancies originating from single trajectories, we resort to time and ensemble-averaged mean square displacement (MSD) to account for the collective diffusion behavior. As illustrated in the temporal evolution of the MSD presented in the inset of Fig. 3c, fluctuations observed in individual trajectories are effectively averaged out, resulting in a relatively Fickian diffusion process with $\mathrm{MSD} = 4Dt$ for short time $t < 0.5-1$ s. Comparing treatment for 5 and 10 s' irradiation, we do observe a significant difference in the ensemble-averaged diffusion coefficient, with $D = 8.7 \times 10^{-14}\,\mathrm{m^2s^{-1}}$ and $D = 1.2 \times 10^{-14}\,\mathrm{m^2s^{-1}}$ for the blue and red curve, respectively. This decrease in proton mobility can be equivalently seen as an increase in the frictional interaction of the protons with the surface, characterized by a friction coefficient $\xi = k_BT/D$, equal respectively to $\xi = 4.7 \times 10^{-8}\,\mathrm{kg\,s^{-1}}$ and $\xi = 3.4 \times 10^{-7}\,\mathrm{kg\,s^{-1}}$.

We can subsequently probe the overall evolution of interfacial mobility as a function of plasma treatment, the results of which are presented in Fig. 3c, reported both as an averaged diffusion coefficient (left axis) and an effective friction coefficient (right axis). The scattered data points were obtained from tens of independent experiments performed on different flakes, with the surface treatment following the same protocols. As evidenced here, we observe a large reduction of surface mobility upon increasing plasma duration, which may be attributed to an elevated trap density that impedes proton jumping.

Non-Gaussian yet Fickian transport process

Following the aforementioned observations, we propose an underlying mechanism responsible for surface-regulated proton transport. We first examine the statistical distributions of the jumping displacement and show that the proton dynamics on the hBN surface is a Fickian process, while its jumping displacement shows a non-Gaussian distribution characterized by a central Gaussian and a side exponential decay.

We focus here on a flake submitted to a short-time plasma treatment, resulting in relatively large mobility, and we imaged for 180,000 frames to increase trajectory statistics. To analyze in more detail the statistical properties of the observed random walks, we plot in Fig. 4a the distribution of hopping displacement at various observation time steps, Δt. A central Gaussian-like distribution, with a constant standard deviation σ typically ~20 nm, is revealed consistently for all Δt. The apparent independence of this central distribution on Δt implies that it is associated with time-invariant events which are likely due to the local trappings evidenced in Figs. 2 and 3. We anticipate that the shape of this central peak stems from a combination of localization errors of the single-molecule detection technique and jiggling motions of the trapped charges on the local clusters. Opposite to this behavior at short displacement, the long-tail arms of these distributions show a pronounced

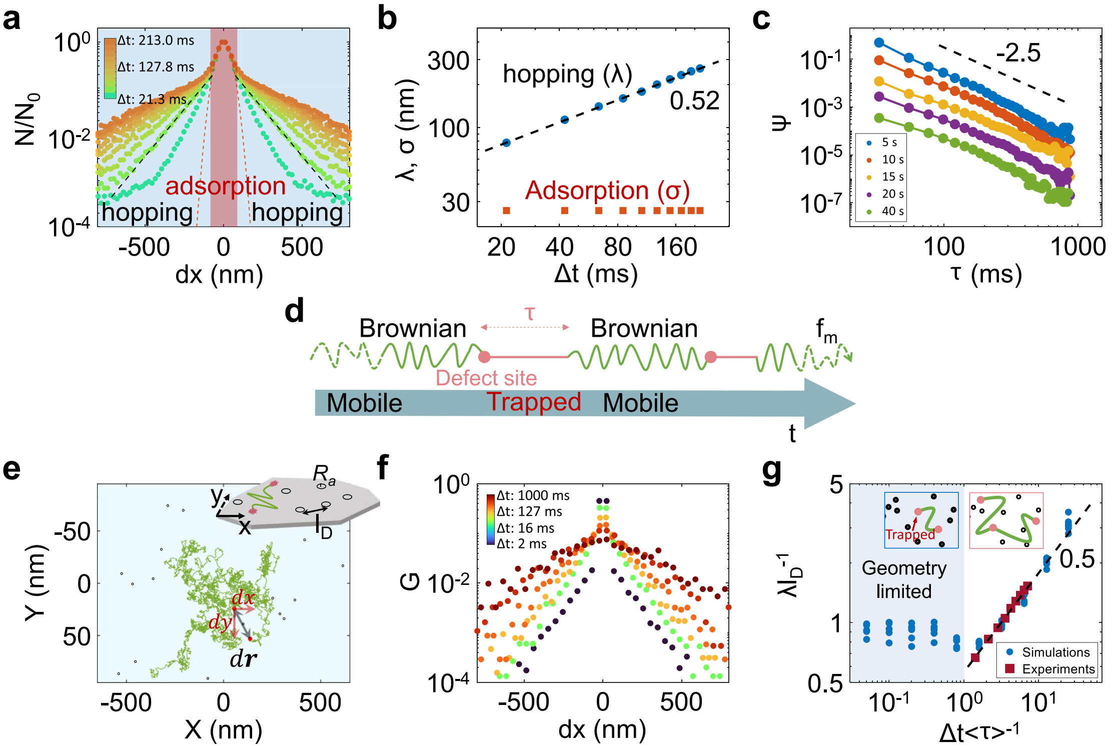

Fig. 4 | Non-Gaussian yet Fickian diffusion process. **a** Histogram showing the normalized distribution of jumping displacement for increasing sampling time, Δt, from 21.3 ms (green) to 213.0 ms (orange) as integer multiples (n) of the initial sampling time (τ_{exp}) with $\Delta t = n\tau_{\mathrm{exp}}$. Red and black dotted lines indicate the Gaussian fitting for the central small displacement and the exponential fitting for the side long displacement, respectively. Exponential decay length, λ, is a function of the sampling time Δt. Bin width: 20 nm. **b** Log–log plot of λ and σ as a function of Δt. The dotted line is a power law fitting to λ with a slope of 0.52, close to the Fickian diffusion power 0.5. The red square is the width, σ, of the central Gaussian, showing no evolution with the sampling time. **c** Distribution of τ at different t_{plasma}. Bin size: 21.3 ms. ψ is shifted by a factor of 0.5 for each t_{plasma} from 5 s to 40 s for visual clarity. **d** Schematic of the Brownian random walker problem. The particle exhibits intermittent Brownian random walking between defects. When encountering a defect, the particle is transiently adsorbed for a random period τ. f_m is the molecular frequency. **e** Example trajectory of one Brownian dynamics simulation run. l_{D}, R_a, and $d\mathbf{r}$ are the mean inter-defect distance, adsorption radius and surface displacement, respectively. The red spot marks the adsorption event (not to scale). **f** Simulations: distribution of particle displacement at various Δt [2–1000 ms], represented by different colors. $\langle\tau\rangle$, l_{D} and bin size are 40 ms, 100 nm and 20 nm. **g** Dimensionless log–log plot of λ, normalized by the mean inter-defect distance l_{D}, as a function of Δt, normalized by $\langle\tau\rangle$. The dotted line is a power fitting to simulations with a slope of 0.5, reminiscent of the Fickian diffusion power law. The two insert schematics show the proton trajectories at two regimes separated by the condition on jumping frequency $\Delta t\langle\tau\rangle^{-1}\sim 1$.

evolution, exhibiting a clear widening for increasing Δt. This behavior is a clear signature of a diffusive-like transport process, where the distance explored by jumping particles becomes longer as the observation time increases. Phenomenologically, this distribution can be approximated by an ad hoc exponentially decaying function, with the probability density $P(|dx|)$ varying as

$$P(|dx|) \sim \exp\left(-\frac{|dx|}{\lambda}\right) \tag{1}$$

Note that for clarity, the distribution in Fig. 4a is shown by normalizing the probability density to a value of unity at the center distribution. To probe the transport process, we plot in Fig. 4b, the evolution of this exponential decay length, λ, on Δt, which grows as $\lambda \sim \sqrt{\Delta t}$, asserting its diffusive-like nature, while the central width σ remains constant over the observation time. These observations indicate that charge dynamics on the aqueous hBN surface are characterized by a highly non-Gaussian yet Fickian process. Such processes are reminiscent of similar behaviors observed in other systems, including colloidal beads in entangled actin suspensions[20,21] and polymer chains' surface dynamics at low molecular weight[46,47]. A traditional description for such exponential distributions is to interpret the non-Gaussian diffusion as being due to the convolution of Gaussian series, which represents the normal modes of microscopic fluctuations[20,21]. Nevertheless, an exact relation between the observed non-Gaussian process and its microscopic origin is still lacking. We propose below a simpler interpretation for this empirical observation, rooted in the microscopic spatial distribution of defects.

We decipher the proton charge dynamics in the framework of the continuous-time random walk (CTRW), in which particles are described as alternating between trapped periods, characterized by a random adsorption time τ, followed by long-distance jumps. In order to quantify the adsorption time distribution, we define a critical jumping displacement, $l_c = 80$ nm, to find the residential events ($|d\mathbf{r}| < l_c$) and the hopping events ($|d\mathbf{r}| > l_c$), from which we statistically estimate residential time distributions from the ensemble trajectories, shown in Fig. 4c. The selection of l_c is based on the localization uncertainty and mean cluster size, and it makes negligible effect on their distributions[46]. Due to our definition based on a critical jumping threshold and to the spatial repartition of the active site in the form of a cluster, adsorption events will characterize not only adsorption at single-defect sites but also at clusters.

A situation where desorption is characterized by a single energy barrier, would lead to an exponential distribution of the residence time[21,29,35,46,47]. However, as shown in Fig. 4c, the distribution of adsorption time τ rather follows a power-law scaling, as $\psi(\tau) \sim \tau^{-\alpha}$ with the exponent $\alpha \simeq 2.5$, suggesting the presence of a broad distribution of desorption energies[21]. The heterogeneity in defect structure evidenced in Fig. 2 suggests that such a distribution might originate at least in part from spatial heterogeneity and defect-to-defect or cluster-to-cluster variations. However, non-exponential distributions in desorption times might also arise at the single-emitter level[48], due e.g., to complex charge escape processes or fluctuations in the local environment. Disentangling the respective contributions of these intrinsic and extrinsic heterogeneities might be a valuable direction for future studies. Interestingly, the value of α obtained here is exactly the same as that in other systems where the size of particles differs from ours by several orders' magnitude[46,47,49], suggesting the universality of this peculiar power-law distribution, whose origin still remains to be uncovered.

To elucidate the microscopic origin of the exponential tails of the jumping displacement, and its evolution with observation time, we conducted 2D Brownian dynamics simulations in the framework of the CTRW, illustrated in Fig. 4d: Protons explore freely the 2D space at the aqueous hBN surface, obeying a standard Brownian dynamics with Gaussian distributed elemental steps. Once the simulated proton meets an active defect site, it is temporarily trapped and ceases to move for a random adsorption time before its next walking step. To simplify the simulations, we neglect site-to-site heterogeneities and draw the adsorption time at each defect site from an effective power-law distribution, as discussed above. Proton displacement is tracked according to such adsorption events, shown by the red dots in Fig. 4e. More details can be found in the Methods section: Brownian dynamics simulations.

We report in Fig. 4f the resulting simulated hopping displacement distribution by varying sampling time Δt (more extensive results in Supplementary Fig. 4). Remarkably, we recover the main features as in our experiments shown in Fig. 4a, with a bimodal distribution characterized by a central peak, corresponding to local adsorption and localization uncertainty, and long distance exponentially decaying tails, associated with inter-defect transport. We note that the central peak in our simulations does not directly reflect the confined motion of protons because experimentally it comes from the localization uncertainty and possibly confined dynamics inside clusters[46,49–51].

Regarding the exponential arms, they are in high synchronization with the experimental observations, exhibiting widening when increasing Δt. We note that our simulation is in stark contrast to the majority of previous simulations, where a power/exponential law distribution of the elemental jumping displacement is pre-assumed[46,47,49,51]. In our case, the single proton jumps at molecular frequency, and the associated displacement obeys a free Gaussian distribution during transport between defects, naturally giving rise to an exponential distribution due to the interaction with the defects. The observed localization events correspond to the adsorption on the active defect site, and the non-Gaussian displacement revealed here is strongly reminiscent of the empirical displacement pre-defined elsewhere[46,47,49,51]. Such a simulation provides evidence that, in the context of our system, the exponential distribution can originate from the intermittent hopping between surface adsorption sites. However, a direct interpretation of such displacement distributions in other contexts should consider the specificity of each systems.

Focusing on the exponential decay length, we show the evolution of the typical decay length λ with the sampling time in Fig. 4g. Note that this length is normalized by the mean inter-defect distance, l_D, defined from the defect density ρ as $l_D = \rho^{-1/2}$, a parameter whose effect we will address in more detail in the next section. Notably, two regimes are evidenced in Fig. 4g, depending on the relative value of the observation time Δt with the mean adsorption time $\langle\tau\rangle$. We argue that this transition originates from the limited adsorption of protons at the defect sites. As depicted by the schematic insert on the right, for $\Delta t > \langle\tau\rangle$, protons can jump between various adsorption sites during the observation time Δt, leading to a diffusive-like feature from which we recover the Fickian behavior $\lambda \sim \sqrt{\Delta t}$, in the same fashion that is experimentally evidenced in Fig. 4b. The dimensionless plot of the exponential decay length on the sampling time in experiments agrees well with simulations, when λ takes the value of 140 nm, a reasonable value for the inter-defect distance[28], which validates our simulation protocols and further strengthen our claim of the molecular origin of the exponential distributions. As depicted by the insert schematic on the left, for $\Delta t < \langle\tau\rangle$, most protons are either immobile between each frame or visit at most one site, corresponding to the shaded geometry-limited regime in Fig. 4g. As a consequence, the hopping displacement becomes independent of Δt and corresponds to the distribution of distance to reach the first encountered defect.

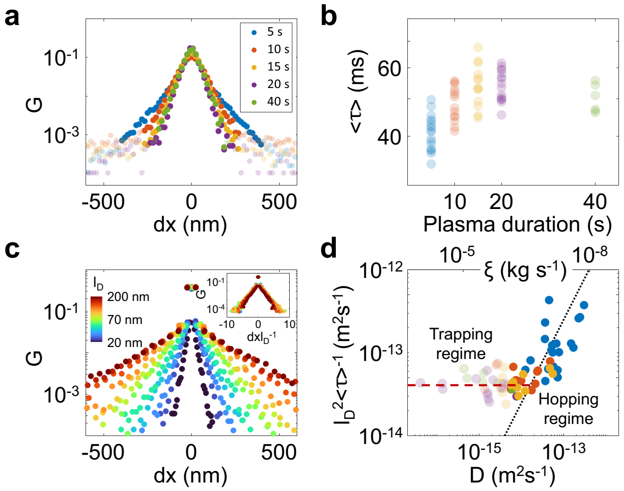

Fig. 5 | Proton dynamics modulated by surface defects. a Distributions of proton jumping displacement on the aqueous hBN surfaces treated by plasma at different t_{plasma}. **b** Experimental averaged adsorption time $\langle\tau\rangle$ at different t_{plasma} for each flake. **c** Simulations: distribution of the proton displacement between each frame at various inter-defect distances [20–200 nm], indicated by different colors. The observation window and the adsorption time are set to be 20 ms and 40 ms, respectively. Insert: distribution of the proton displacement normalized by the inter-defect distance. **d** Plot of the diffusion coefficient D and friction coefficient ξ as a function of the averaged inter-defect distance l_D and the averaged adsorption time $\langle\tau\rangle$. The scattered points are from experiments, and the semi-transparent and solid data points correspond to the trapping regime and the hopping regime. The black dotted line is the scaling relation from the Brownian dynamics simulations, expected from the desorption-mediated model[30,44,52], where the hopping dominates the displacement distributions. The red dotted line is estimated from the converging distributions of the displacement and represents the trapping regime where most protons are locally trapped at the adsorption sites.

Defect-modulated transport and ionic friction

In light of the displacement distributions discussed above, we proceed to examine in more detail the dependence of hopping statistics on irradiation time t_{plasma}, which sets the local defect landscape. We report in Fig. 5a the typical evolution of the hopping displacement for distinct t_{plasma} at a fixed sampling time $\Delta t = 20$ ms. Increasing t_{plasma} from 5 to 40 s leads to a clear narrowing of the distribution, consistent with a reduced probability for long displacement, and a reduction of the diffusion coefficient D, evidenced in Fig. 3c.

Alongside the qualitative analysis made in Fig. 3a, another interpretation of the above findings is to inspect the adsorption site morphology from the accumulated emission events, summarized in Fig. 2. The density of clusters increases with t_{plasma}, indicating a greater prevalence of the trapped trajectories, as shown in Fig. 2e. Moreover, the ratio of the localization density corresponding to the immobile state to that of the mobile state increases with an increase in t_{plasma}, as illustrated in Fig. 2f. In addition, the mean adsorption period increases with plasma duration, effectively slowing down the proton transport as shown in Fig. 5b. These findings suggest that protons exhibit reduced mobility on flakes at larger t_{plasma} that port more defects.

To clarify this behavior in a quantitative way, we carried out additional Brownian dynamics simulations, probing specifically the role of spatial defect distribution, characterized by the mean inter-defect distance, on jumping displacement. To seek a simple mechanism, we assume that the plasma treatment only modifies the defect morphology but not the other physicochemical properties of the surface. As shown in Fig. 5c, upon increasing l_D (going from black to red distributions), we observe a clear broadening of the exponential arms, consistent with longer jumping displacement. This effect is in accordance with our experimental observations in Fig. 5a: shorter plasma induces fewer defects and hence larger l_D, which broadens the displacement distribution. Furthermore, the distributions at various l_D collapse onto the same master curve once the displacement is normalized by l_D as shown by the insert on Fig. 5c, implying the strong influence of the surface defects, whose estimation will be discussed in details in the next. Interestingly, we recover an empirical scaling for the ensemble diffusion, $D \sim l_D^2 \langle\tau\rangle^{-1}$ expected by the desorption-mediated transport[30,44,52,53], with a thorough report of the effect of the $\langle\tau\rangle$ and l_D in Supplementary Figs. 4–6. We note that this relation holds regardless of the values assigned to l_D and $\langle\tau\rangle$, demonstrating the robust nature of our molecular interpretation.

Once the above semi-empirical relation is injected into the Fickian equation, $\lambda \sim \sqrt{D\Delta t}$, we obtain the following dimensionless relation, $\lambda/l_D \sim \left(\Delta t/\langle\tau\rangle\right)^{1/2}$, that is precisely reproduced by our simulations and corresponds to the experimental observations in Fig. 4g. Coming back to the distribution of hopping displacements, they should similarly collapse onto the same master curve when normalized by l_D at fixed Δt and $\langle\tau\rangle$, a process that is exactly reproduced by our simulations shown by the insert in Fig. 5c.

We now comment on the experimental estimation of two pivotal parameters, as the typical inter-defect distance l_D and the average adsorption time $\langle\tau\rangle$. τ is detected with the same protocols as described in the last section, and its average $\langle\tau\rangle$ is subsequently statistically summarized in Fig. 5b. Each data point represents the independent experimental result obtained from one single flake. The broad dispersion of the experimental data is attributed to the inherent heterogeneity of each flake. It is yet evident that $\langle\tau\rangle$ shows a slight increase with the duration of the plasma exposure. This finding is in accordance with the report on the cumulant photoluminescent sites in Fig. 2e, f, which reveals an increase in the number of clusters and immobile events for cases involving a longer t_{plasma}. When t_{plasma} is longer than 15 s, most of the protons are thus locally trapped, and it appears that $\langle\tau\rangle$ reaches a saturation.

Coming back to the question of the defect density and inter-defect distance, estimating such values is notoriously difficult. Previous attempts include direct measurements through Transmission Electron Microscopy[54] or tracking of cumulant photoluminescent sites[28]. Those methods either change the surface state during their implementation or require long tracking with complex approaches to correct spatial drifting. To seek a simple, reliable approach, we propose here to extrapolate a typical inter-defect distance l_D based on the exponential decay length λ, thanks to the peculiarity of the exponential distribution of jumping displacement, by taking $l_D \simeq \lambda$, when $\langle\tau\rangle \approx \Delta t$, as is the case in our experiments (see the Supplementary: Section 6). Such estimation has the merit of avoiding an exhaustive (and sometimes ambiguous) exploration of all the surface defects, as is necessary for the cumulant tracking[28].

We revert to the ensemble diffusion coefficient and compare it with our experimental estimation of l_D and $\langle\tau\rangle$. As shown in Fig. 5d, we find a reasonable concordance between these experimentally defined parameters and the simple scaling law $D \sim l_D^2 \langle\tau\rangle^{-1}$ for the larger mobility samples (black dotted line). However, for the lower diffusion coefficients corresponding to the longer plasma treatments, we observe a breakdown of this scaling, with $l_D^2 \langle\tau\rangle^{-1}$ becoming independent of D. This breakdown is concomitant with the convergence of the hopping distribution in Fig. 5a towards an exponential distribution of characteristic length $\lambda_c \approx 40$ nm at large plasma treatment times, equivalently shown by the red dotted line in Fig. 5d. In this limit, the majority of protons are locally adsorbed on the cluster sites with very rare inter-cluster transport. Such confined motion leads to a strong drop of the effective diffusion coefficient (Fig. 3c), while the exponential jumping distributions converge towards finite values due to the uncertainty in the localization precision combined with confined jumps inside clusters.

Finally, we comment on the interfacial friction associated with proton transport observed in our experiments. As discussed earlier, the ensemble diffusion coefficient D can also be related to an effective friction coefficient ξ, which characterizes the effective dissipative frictional force, $\mathbf{F} = \xi\mathbf{v}$, experienced by a charged particle moving at a drift velocity $\mathbf{v}$, under linear response theory. These two quantities are related via the fluctuation-dissipation relation, $D \sim k_BT/\xi$. Interestingly, the lowering of the diffusion coefficient at high defect density is thus equivalently expressed as an increasing frictional interaction felt by single charges with the surface. The observed phenomenology of a discontinuous transport limited by escape from deep traps bears an analogy to the discontinuous stick-slip motion encountered in single-asperity sliding in nanotribology systems[55], evidenced here at the single molecule scale. Yet a key difference would lie in the broad distribution of trapping energies and trapping time evidenced in our system, which would be expected to give rise to richer and more complex transport behaviours.

Conclusions

In this work, we resorted to a single-molecule localization technique to uncover the key role played by surface defects in regulating single charge transport at the aqueous hBN interface. Probing the local distribution of plasma-induced defects through super-resolution mapping reveals the presence of two types of morphologies for the adsorption sites, with sparsely distributed and weakly adsorbing sites coexisting with dense and strongly adsorbing defect clusters. We then focus on the study of single charge dynamics in such a defective landscape by harvesting the spatio-temporal correlations in nearby defect activation to track the hopping motion of a single charge between defects. We observe that longer plasma treatment impedes the mobility, which we ascribe at a qualitative level to an increase in defect density leading to increasing frictional interactions. To further quantify transport, we analyze in more detail the observed trajectories, reminiscent of continuous-time random walk processes, and the associated distribution of hopping displacements in which a central adsorption peak coexists with an exponentially decaying arm associated with inter-defect transport. To elucidate the origin of this bimodal distribution, we resort to Brownian dynamics simulations of freely diffusing 2D Brownian particles in a defective landscape composed of homogeneously distributed adsorbing sites. This simple modeling approach evidences that the long-distance exponentially decaying arms arise naturally due to transport between nearby defects and scale with the inter-defect distance, while the central Gaussian peak can be ascribed to the charge adsorption at the strong trapping sites. We further present a simple scaling law relating the interfacial ensemble diffusion coefficient to the mean defect adsorption period and inter-defect distance, which compares favorably with our experimental data in the high mobility regime associated with short plasma treatments. We finally link the ensemble diffusion coefficient to interfacial ionic friction, demonstrating the control of molecular-scale dissipation at the nanoscale. We stress that our analysis throughout employs no free fitting parameters, reinforcing our claim for the molecular origin of the exponentially decaying single charge jumps between defect sites and the control of mobility and interfacial friction, with surface defects.

Our findings open up new insights on the role of defects in interfacial proton transport, an overlooked parameter of importance for a variety of fields involving ionic transport at solid/liquid interfaces. These advances further establish a new step towards the understanding of collective particle transport at aqueous interfaces from single-molecule dynamics and open new avenues for investigating atomistic friction and dissipative effects at solid-liquid boundaries. Building upon the current findings and our previous results[30,35], future work could explore in greater depth the interplay between pH, defect activity, and proton diffusion dynamics. Although the present study focuses exclusively on protons, the broader framework of defect and adsorption modulated interfacial transport developed here may be applicable to other ionic species-particularly those exhibiting strong surface interactions. Extending this methodology to exogenous ions, such as metal cations, would represent an exciting direction[33].

Methods

Single-molecule microscopy setup

Single-molecule tracking experiments were performed using a custom-made single-molecule localization microscope, build around an inverted

Table 1 | Simulation parameters

Mean inter-defect distance l_D (nm)	Mean adsorption time $\langle \tau \rangle$ (ms)	Exposure time Δt (ms)
2–200	1–150	2–1000

microscope (IX83, Olympus). The hBN flake was mounted on a custom-designed holder compatible with a high-numerical-aperture oil-immersion objective (Olympus TIRFM 100×, NA 1.5, UPLAPO100XOHR) and excited with a 561 nm laser (LCX-561L-100-CSB-PPF, Oxxius). The excitation power measured at back focal plane of the objective was around 10 mW, resulting in a power density of approximately 0.5 $kW.cm^{-2}$. Photoluminescence signal emitted from the excited sample was collected through the same oil-immersion objective. Fluorescent emission was separated and filtered using dichroic and emission filters (Semrock Di03-R405/488/561/635 and FF01-446/523/600/677). The resulting emission signal was projected onto an EMCCD camera (iXon Ultra, Andor, with an EM gain of 150), following magnification by a factor 1.4X, leading to a projected pixel size of 114.3 nm.

Brownian dynamics simulations

Single protons are assumed to explore freely the 2D space at the aqueous hBN surface, obeying a standard Brownian motion with Gaussian distributed elemental steps. The proton jumps at a molecular frequency that we set to 10^{10} Hz with the bulk diffusion coefficient $\sim 10^{-8}\ m^2 s^{-1}$ [56,57]. We consider randomly distributed defects, with fixed density ρ, from which we define an interdefect distance $l_D = \rho^{-1/2}$. Defects are modeled by an adsorbing boundary with an interaction radius $R_a \approx 1$ nm, which characterizes the typical range of interactions between the diffusing charge and the surface defect. We note that this interaction radius is not far from the Bjerrum length of 0.7 nm characterizing the typical range of electrostatic interactions in our experimental conditions, which would presumably be involved in the trapping of a proton to the negatively charged V_B^- vacancy. In a typical simulation run, the Brownian particle starts close to a random defect site (at a distance $2R_a$). The particle diffuses freely on the surface until it encounters a defect. An adsorption event takes place when the Brownian particle enters within R_a of a nearby defect site, following which the particle becomes locally trapped at the defect site for a random adsorption time τ. We take this trapping period as obeying the power law $\psi(\tau) \sim \tau^{-2.5}$ with its mean value measured from experiments, before it takes the next hopping. We can simulate the effective random walks as a succession of trapping events with key adjustable simulation parameters listed in Table 1, covering the scope of our experimental observations. Other numerical parameters, including the molecular jumping frequency and the attraction radius, show almost negligible effect on the proton dynamics (Supplementary Fig. 8).

Data availability

The authors declare that the data supporting the findings of this study are available within the paper and its supplementary information files.

Received: 12 March 2025; Accepted: 30 July 2025;

References

1. Tajkhorshid, E. et al. Control of the selectivity of the aquaporin water channel family by global orientational tuning. *Science* **296**, 525–530 (2002).
2. Wadhwa, N. & Berg, H. C. Bacterial motility: machinery and mechanisms. *Nat. Rev. Microbiol.* **20**, 161–173 (2022).
3. Siria, A., Bocquet, M.-L. & Bocquet, L. New avenues for the large-scale harvesting of blue energy. *Nat. Rev. Chem.* **1**, 0091 (2017).
4. Zhang, Z., Wen, L. & Jiang, L. Nanofluidics for osmotic energy conversion. *Nat. Rev. Mater.* **6**, 622–639 (2021).
5. Esfandiar, A. et al. Size effect in ion transport through angstrom-scale slits. *Science* **358**, 511–513 (2017).
6. Gopinadhan, K. et al. Complete steric exclusion of ions and proton transport through confined monolayer water. *Science* **363**, 145–148 (2019).
7. Ruiz-Lopez, M. F., Francisco, J. S., Martins-Costa, M. T. & Anglada, J. M. Molecular reactions at aqueous interfaces. *Nat. Rev. Chem.* **4**, 459–475 (2020).
8. Lis, D., Backus, E. H., Hunger, J., Parekh, S. H. & Bonn, M. Liquid flow along a solid surface reversibly alters interfacial chemistry. *Science* **344**, 1138–1142 (2014).
9. Tarun, O. B., Hannesschläger, C., Pohl, P. & Roke, S. Label-free and charge-sensitive dynamic imaging of lipid membrane hydration on millisecond time scales. *Proc. Natl. Acad. Sci.* **115**, 4081–4086 (2018).
10. Mouterde, T. et al. Molecular streaming and its voltage control in ångström-scale channels. *Nature* **567**, 87–90 (2019).
11. Allemand, A. et al. Anomalous ionic transport in tunable angstrom-size water films on silica. *Proc. Natl. Acad. Sci.* **120**, e2221304120 (2023).
12. Ricci, M., Spijker, P. & Voítchovsky, K. Water-induced correlation between single ions imaged at the solid–liquid interface. *Nat. Commun.* **5**, 4400 (2014).
13. Martin-Jimenez, D., Chacon, E., Tarazona, P. & Garcia, R. Atomically resolved three-dimensional structures of electrolyte aqueous solutions near a solid surface. *Nat. Commun.* **7**, 12164 (2016).
14. Tunuguntla, R. H. et al. Enhanced water permeability and tunable ion selectivity in subnanometer carbon nanotube porins. *Science* **357**, 792–796 (2017).
15. Siria, A. et al. Giant osmotic energy conversion measured in a single transmembrane boron nitride nanotube. *Nature* **494**, 455–458 (2013).
16. You, Y. et al. Angstrofluidics: walking to the limit. *Annu. Rev. Mater. Res.* **52**, 189–218 (2022).
17. Robin, P. & Bocquet, L. Nanofluidics at the crossroads. *J. Chem. Phys.* **158**, 160901 (2023).
18. Aluru, N. R. et al. Fluids and electrolytes under confinement in single-digit nanopores. *Chem. Rev.* **123**, 2737–2831 (2023).
19. Pagliero, D. et al. Slow water in engineered nanochannels revealed by color-center-enabled sensing. *Nano Lett.* **25**, 9960–9966 (2025).
20. Wang, B., Anthony, S. M., Bae, S. C. & Granick, S. Anomalous yet brownian. *Proc. Natl. Acad. Sci.* **106**, 15160–15164 (2009).
21. Wang, B., Kuo, J., Bae, S. C. & Granick, S. When brownian diffusion is not Gaussian. *Nat. Mater.* **11**, 481–485 (2012).
22. Alexandre, A. et al. Non-Gaussian diffusion near surfaces. *Phys. Rev. Lett.* **130**, 077101 (2023).
23. Waigh, T. A. & Korabel, N. Heterogeneous anomalous transport in cellular and molecular biology. *Rep. Prog. Phys.* **86**, https://doi.org/10.1088/1361-6633/ad058f (2023).
24. Faucher, S. et al. Critical knowledge gaps in mass transport through single-digit nanopores: a review and perspective. *J. Phys. Chem. C.* **123**, 21309–21326 (2019).
25. Kavokine, N., Netz, R. R. & Bocquet, L. Fluids at the nanoscale: from continuum to subcontinuum transport. *Annu. Rev. Fluid Mech.* **53**, 377–410 (2021).
26. Bocquet, L. Nanofluidics coming of age. *Nat. Mater.* **19**, 254–256 (2020).
27. Tran, T. T., Bray, K., Ford, M. J., Toth, M. & Aharonovich, I. Quantum emission from hexagonal boron nitride monolayers. *Nat. Nanotechnol.* **11**, 37–41 (2016).
28. Feng, J. et al. Imaging of optically active defects with nanometer resolution. *Nano Lett.* **18**, 1739–1744 (2018).
29. Comtet, J. et al. Wide-field spectral super-resolution mapping of optically active defects in hexagonal boron nitride. *Nano Lett.* **19**, 2516–2523 (2019).
30. Comtet, J. et al. Direct observation of water-mediated single-proton transport between hbn surface defects. *Nat. Nanotechnol.* **15**, 598–604 (2020).
31. Caldwell, J. D. et al. Photonics with hexagonal boron nitride. *Nat. Rev. Mater.* **4**, 552–567 (2019).

32. Ronceray, N. et al. Liquid-activated quantum emission from pristine hexagonal boron nitride for nanofluidic sensing. *Nat. Mater.* **22**, 1236–1242 (2023).
33. Wu, Y. et al. Single-ion spectroscopy of h-bn point defect fluorescence in liquid environments. *arXiv* https://arxiv.org/abs/2407.01934 (2024).
34. Zhang, M., Lozano, C. I., van Veen, S. & Albertazzi, L. Label-free identification of biomolecules by single-defect-spectroscopy at the aqueous hexagonal boron nitride interface. *arXiv* https://arxiv.org/abs/2409.18702 (2024).
35. Comtet, J. et al. Anomalous interfacial dynamics of single proton charges in binary aqueous solutions. *Sci. Adv.* **7**, eabg8568 (2021).
36. Mayner, E. et al. Monitoring electrochemical dynamics through single-molecule imaging of hbn surface emitters in organic solvents. *ACS Nano* **18**, 27401–27410 (2024).
37. Bocquet, L. & Barrat, J.-L. Flow boundary conditions from nano-to micro-scales. *Soft matter* **3**, 685–693 (2007).
38. Joly, L., Tocci, G., Merabia, S. & Michaelides, A. Strong coupling between nanofluidic transport and interfacial chemistry: how defect reactivity controls liquid–solid friction through hydrogen bonding. *J. Phys. Chem. Lett.* **7**, 1381–1386 (2016).
39. Seal, A. & Govind Rajan, A. Modulating water slip using atomic-scale defects: friction on realistic hexagonal boron nitride surfaces. *Nano Lett.* **21**, 8008–8016 (2021).
40. Xie, Y., Fu, L., Niehaus, T. & Joly, L. Liquid-solid slip on charged walls: the dramatic impact of charge distribution. *Phys. Rev. Lett.* **125**, 014501 (2020).
41. Döpke, M. F., Westerbaan van der Meij, F., Coasne, B. & Hartkamp, R. Surface protolysis and its kinetics impact the electrical double layer. *Phys. Rev. Lett.* **128**, 056001 (2022).
42. Hugelier, S., Colosi, P. & Lakadamyali, M. Quantitative single-molecule localization microscopy. *Annu. Rev. Biophys.* **52**, 139–160 (2023).
43. Grosjean, B., Bocquet, M.-L. & Vuilleumier, R. Versatile electrification of two-dimensional nanomaterials in water. *Nat. Commun.* **10**, 1656 (2019).
44. Springer, A., Hagen, V., Cherepanov, D. A., Antonenko, Y. N. & Pohl, P. Protons migrate along interfacial water without significant contributions from jumps between ionizable groups on the membrane surface. *Proc. Natl. Acad. Sci.* **108**, 14461–14466 (2011).
45. Weichselbaum, E. et al. Origin of proton affinity to membrane/water interfaces. *Sci. Rep.* **7**, 4553 (2017).
46. Skaug, M. J., Mabry, J. N. & Schwartz, D. K. Single-molecule tracking of polymer surface diffusion. *J. Am. Chem. Soc.* **136**, 1327–1332 (2014).
47. Skaug, M. J., Mabry, J. & Schwartz, D. K. Intermittent molecular hopping at the solid-liquid interface. *Phys. Rev. Lett.* **110**, 256101 (2013).
48. Kuno, M., Fromm, D. P., Hamann, H. F., Gallagher, A. & Nesbitt, D. J. Nonexponential "blinking" kinetics of single cdse quantum dots: a universal power law behavior. *J. Chem. Phys.* **112**, 3117–3120 (2000).
49. Sarfati, R. & Schwartz, D. K. Temporally anticorrelated subdiffusion in water nanofilms on silica suggests near-surface viscoelasticity. *ACS Nano* **14**, 3041–3047 (2020).
50. Wong, I. Y. et al. Anomalous diffusion probes microstructure dynamics of entangled f-actin networks. *Phys. Rev. Lett.* **92**, 178101 (2004).
51. Chaudhuri, P., Berthier, L. & Kob, W. Universal nature of particle displacements close to glass and jamming transitions. *Phys. Rev. Lett.* **99**, 060604 (2007).
52. Reed, D. A. & Ehrlich, G. Surface diffusion, atomic jump rates and thermodynamics. *Surf. Sci.* **102**, 588–609 (1981).
53. He, Y., Burov, S., Metzler, R. & Barkai, E. Random time-scale invariant diffusion and transport coefficients. *Phys. Rev. Lett.* **101**, 058101 (2008).
54. Rasool, H. I., Ophus, C. & Zettl, A. Atomic defects in two dimensional materials. *Adv. Mater.* **27**, 5771–5777 (2015).
55. Vanossi, A., Manini, N., Urbakh, M., Zapperi, S. & Tosatti, E. Colloquium: modeling friction: from nanoscale to mesoscale. *Rev. Mod. Phys.* **85**, 529–552 (2013).
56. Agmon, N. The grotthuss mechanism. *Chem. Phys. Lett.* **244**, 456–462 (1995).
57. Knight, C. & Voth, G. A. The curious case of the hydrated proton. *Acc. Chem. Res.* **45**, 101–109 (2012).
58. Scott, D. W. Averaged shifted histograms: effective nonparametric density estimators in several dimensions. *Ann. Stat.* **13**, 1024–1040 (1985).

Acknowledgements

M.Z. and J.C. acknowledge funding from the ANR (grant 'GUACAmole' ANR-22-CE06-0003-01), and the Ile-de-France Region in the framework of 'DIM Respore' and 'DIM MaTerRE'. This project has also received financial support from the CNRS through the MITI interdisciplinary programs and from the Carnot Institute 'IPGG Microfluidique'. M.Z. acknowledges further support from the National Natural Science Foundation of China (grant No.: 12388101), K.W. and T.T. acknowledge support from the JSPS KAKENHI (grant No.: 21H05233 and 23H02052), the CREST (grant No.: JPMJCR24A5), JST and World Premier International Research Center Initiative (WPI), MEXT, Japan.

Author contributions

M.Z. and J.C. designed the research. M.Z. performed the experiments and processed the data. M.Z. and J.C. analyzed the data and wrote the paper. M.Z. conducted the simulations with the help of J.C., K.W., and T.T. contributed the materials. J.C. supervised the project. All authors discussed the results and commented on the manuscript.

Competing interests

The authors declare no competing interests.

Additional information

Supplementary information The online version contains supplementary material available at https://doi.org/10.1038/s43246-025-00910-3.

Correspondence and requests for materials should be addressed to Jean Comtet.

Peer review information *Communications Materials* thanks Hiroaki Yoshida, Yecun Wu and the other, anonymous, reviewer(s) for their contribution to the peer review of this work. Primary Handling Editors: Jet-Sing Lee. [A peer review file is available].